ADVANCED ENGINEERING MATERIALS
www.aem-journal.com

Illuminating Origins of Impact Energy Dissipation in Mechanical Metamaterials

*Peter Vuyk, Shichao Cui, and Ryan L. Harne**

Elastomeric mechanical metamaterials have revealed striking ability to attenuate shock loads at the macroscopic level. Reports suggest that this capability is associated with the reversible elastic buckling of internal beam constituents observed in quasistatic characterizations. Yet, the presence of buckling members induces non-affine response at the microscale, so that clear understanding of the exact energy dissipation mechanisms remains clouded. In this report, the authors examine a mechanical metamaterial that exhibits both micro- and macroscopic deformations under impact loads and devise an experimental method to visualize the resulting energy dissipation mechanisms. By illuminating the dynamic distribution of strain in the metamaterial, the authors uncover a rational way to program the macroscopic deformation and enhance impact mitigation properties. The results emphasize that mechanical metamaterials clearly integrate materials science and structural engineering, encouraging future interdisciplinary studies to capitalize on the opportunities.

The blow of an impact can rapidly harm people and engineered systems.[1,2] This challenge has fueled development of resilient engineered material systems able to suppress the transmission of impact energy to the shielded body or structure. Recent attention has turned to buckling-based material system concepts, whereby elastic and/or plastic buckling structural members on a microscale level[3–7] are harnessed to absorb shock at the system level. Preferring the reusability of elastic buckling phenomena and the practicality of elastomers, classes of elastomeric mechanical metamaterials have been devised with internal cellular geometries that absorb elastic energy via reversible buckling events in periodic, microscale elastomeric beam constituents.[8–12] Under low frequency cycling of applied strain or stress, these new generations of cellular materials[13] are shown to exhibit exceptional elastic energy dissipation properties[14–16] due to a "reversible plasticity" effect[17] that has an analogy to energy management in cytoskeletal actin networks.[18–21]

Yet, a common vision for elastomeric mechanical metamaterials is to mitigate impact, in which case high strain rates are induced. In this light, experimental evidence suggests these metamaterials are effective to dissipate sudden accelerations[9] and shocks,[11] although the exact energy mitigation mechanisms are unknown. While there are inherent ties between shock absorption mechanisms and the elastic buckling of the beam constituents in such elastomeric metamaterials,[22] when composed into material systems the presence of buckling members gives rise to non-affine response at the microscale that ultimately governs macroscopic energy dissipation properties of the system.[23,24] These internal instabilities break the direct proportionality between micro- and macroscale behaviors.[25] Although high-speed video has shed light on energy transfer and dissipation in similar problems[26,27] (Video S1), there are limitations in the interpretation of video sequences their own. The full illumination of underlying impact energy dissipation mechanisms is needed to formulate understanding that may usher an expanse of future investigations and may propel concepts of elastomeric mechanical metamaterials on to widespread application.

The digital image correlation (DIC) method appears well-suited to meet this need. DIC experiments capture video images that are used to correlate relative displacements of a speckled grid placed over the specimen surface with the displacement and strain fields over the measured surface.[28,29] The local strain corresponds to the local stress, thus illuminating the origins and distributions of energy dissipation. Yet, despite advancements to DIC for measuring shock transmission through stochastic cellular materials like foams[30,31] and 3D-printed lattices,[32] the approach has yet to be translated to explain the working mechanisms of impact energy dissipation in mechanical metamaterials. Because these metamaterials harness significant micro- and macroscale deformations uniquely with respect to stochastic cellular materials, it may be deduced that the local and global behaviors will collectively reveal why elastomeric metamaterials may be so effective at suppressing shock.

To address these gaps in fundamental understanding and experimental capability, we investigate an archetypal elastomeric metamaterial with a constant cross-section geometry composed of uniform vertical beam constituents connected by a horizontal beam (**Figure 1**a, Table S1). This geometry is favorable for our aims because the number of repeated vertical beam unit cells cultivates a combination of collective, macroscopic behavior as well as local, microscopic response under impact loads (Video

Prof. R. L. Harne, P. Vuyk, S. Cui
Department of Mechanical and Aerospace Engineering, The Ohio State University, USA
E-mail: harne.3@osu.edu

The ORCID identification number(s) for the author(s) of this article can be found under https://doi.org/10.1002/adem.201700828.

DOI: 10.1002/adem.201700828

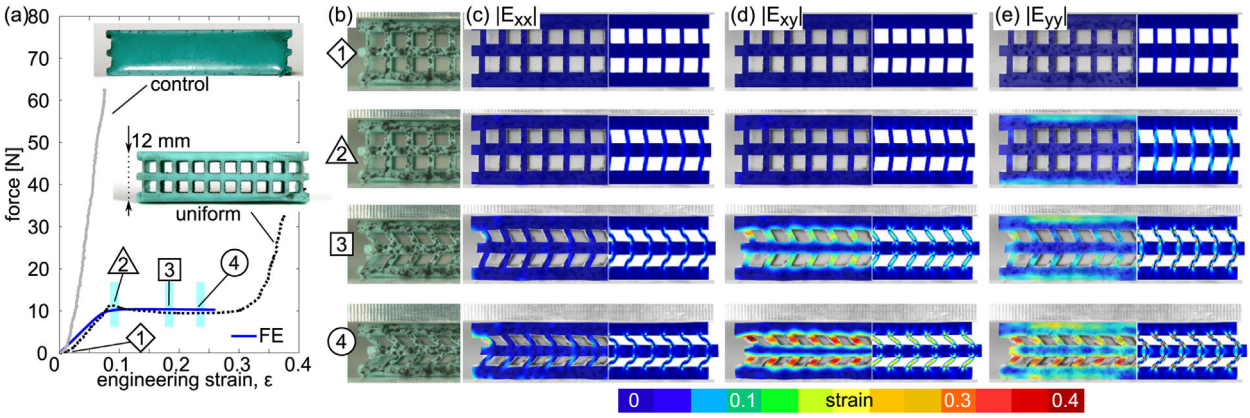

Figure 1. Mechanical properties characterization and evidence of dissipation mechanisms in the metamaterial. a) Force–strain profiles of Control specimen (bulk elastomer) and the Uniform metamaterial, along with FE simulation results for the metamaterial. b) Unprocessed images of the Uniform metamaterial with speckle pattern. c–e) show, respectively, $|E_{xx}|$, $|E_{xy}|$, and $|E_{yy}|$ strains as computed from the DIC data. At right in each part of c–e) are corresponding FE simulation results. The numeric labels in the figure correspond to parts identified in a).

S1). When loaded quasistatically, the mechanical properties of the metamaterial reveal a trilinear trend (Figure 1a) with characteristics similarly observed in other studies of mechanical metamaterials.[16,33] Beyond the small strain, quasi-linear regime, the plateau of force at moderate strains is due to elastic buckling of the vertical beams, followed by self-contact of the cellular cross-section for further strain increase.[34] The uniform metamaterial and control (solid elastomer) specimens serve as baselines against which the impact energy dissipation characteristics of variants of the metamaterial geometry are assessed and elucidated.

We devise a method of speckling the elastomeric specimens in the fabrication and experimental preparation stages so that micro- and macroscale deformations are sufficiently reconstructed when post-processing the high-speed video recordings in our DIC method (see Supporting Information for details, and Figure S1, S2, S6, S7). Subsequently, in the quasistatic loading of the specimens (Figure S4), the relative motions of the speckle particles (Figure 1b) are tracked and correlated to displacement and strain. Figure 1c–e, respectively, show the magnitudes of Green–Lagrangian normal strain in the horizontal direction $|E_{xx}|$, shear strain of the cross-section $|E_{xy}|$, and normal strain in the vertical direction $|E_{yy}|$ for the uniform metamaterial at different extents of macroscopic applied strain in the load frame. The metamaterial deforms with large unilateral motion of the horizontal beam, which induces a collective bending motion of the vertical beams. Consequently, the vertical beams exhibit large shear and vertical compressive strains (Figure 1d, e). This indicates that vertical beam bending in the buckling deformation is the primary mechanism by which energies that induce vertical strain/stress are attenuated in the uniform metamaterial (Video S2). Our FE model results agree with the trends albeit with underprediction of the local strain fields and exaggeration of edge effects (see Supporting Information for details, and Figure S3). On the other hand, the qualitative agreement between FE results and DIC data, especially the increased shear and vertical strains evident in the unilateral deformation characteristics, confirms that our DIC method is viable to map the micro- and macroscopic deformation and strain fields.

We then examine how this damping mechanism translates to the case of impulsive loads. When subjected to repeated impact forces (**Figure 2**a, S5, S8), the peak transmitted output force is related to the peak input force and to the pre-strain ε_0 (engineering strain) applied in securing the metamaterial to the fixture (Figure 2b, S9). The bilinear trend of output force for the metamaterial indicates large impact energy is absorbed by the elastic buckling of the vertical beams prior to beam self-contact for greater input forces. The input force needed to cause the latter densification effect is intuitively reduced when the pre-strain ε_0 is increased via the experimental fixture that may adjust a static vertical compressive force (Figure S5). Clearly the ability of the vertical beams to elastically buckle is a general means by which the blows are absorbed. The linear slopes of the curves that exceed the elastic buckling regime are greater than the slope of the control specimen curve (Table S2), unsurprisingly, due to less material in the densified metamaterial than the control to suppress the transmitted force. Yet, a question remains as to what microscale phenomena occur to absorb such impact energy. Applying our DIC approach to the impact measurements, we discover similar unilateral motion of the horizontal beam in the metamaterial (Figure 2c–e, Video S3) as that observed for quasistatic load (Figure 1c–e). After an initial cascading-type buckling of the vertical beams that briefly heightens local horizontal normal strain (Video S3), the DIC data confirm that the metamaterial with uniform thickness vertical beams undergoes a collective internal buckling behavior and large vertical and shear strain to mitigate the impact energy.

Having established a method to uncover impact energy dissipation mechanisms of the elastomeric metamaterials, we investigate an approach to program the impact mitigation properties via the internal, beam geometries. It is apparent that uniformity of vertical beam thicknesses cultivates a unilateral, collective buckling motion of the metamaterial. To break the perfect periodicity, two metamaterial classes are fabricated as variants of the uniform specimen. The R-class uses a linear increase in the vertical beam thickness from outer to center beams, while the L-class uses a linear increase in vertical beam thickness from inner to outer (Table S1). A-type specimens use

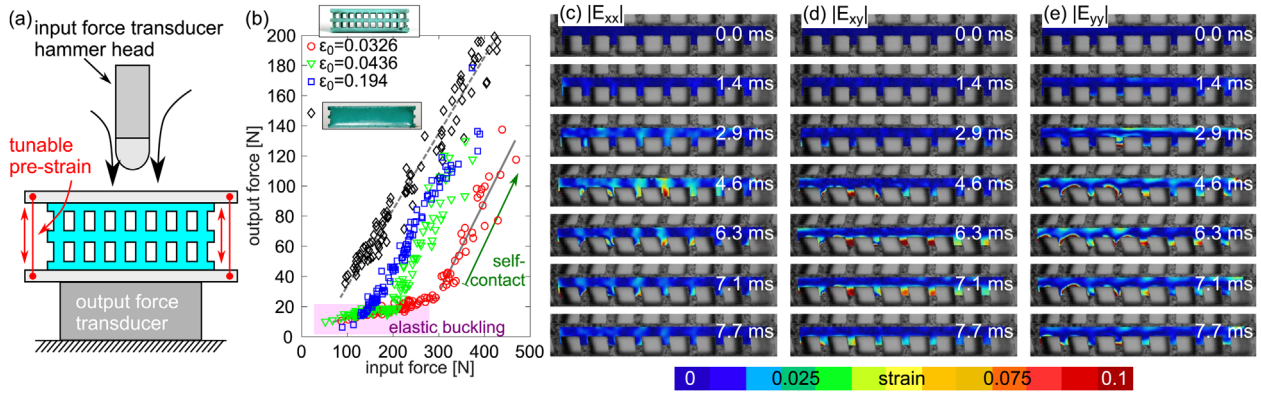

Figure 2. Impact energy mitigation in the Uniform metamaterial. a) Experimental schematic. b) Measurements of output force peak as a function of input impact force peak. For the Control specimen (black diamonds), a linear fit is shown as the dashed line. For the Uniform metamaterial, measurements are shown using different pre-strains. The bilinear fits for the least pre-strained Uniform metamaterial are shown as the light gray solid curves. c–e), respectively, show $|E_{xx}|$, $|E_{xy}|$, and $|E_{yy}|$ strains for an impact force of 148 N on the least pre-strained Uniform metamaterial. The significance of vertical beam bending and unilateral horizontal beam deflection are observed.

less such variation of vertical beam thickness than the B-type specimens in a given class. When loaded quasistatically, the metamaterial classes reveal distinct force-displacement profiles. Indeed, the L-class metamaterials exhibit a region of negative stiffness in the profiles suggestive of internal beam elastic buckling (**Figure 3**f) not seen for the R-class metamaterials (Figure 3a). Yet, the DIC results for the R-B metamaterial confirm that elastic buckling occurs, albeit in a symmetric way about a vertical line through the cross-section, which promotes bimodal horizontal beam deflection (Figure 3b–d). These aspects

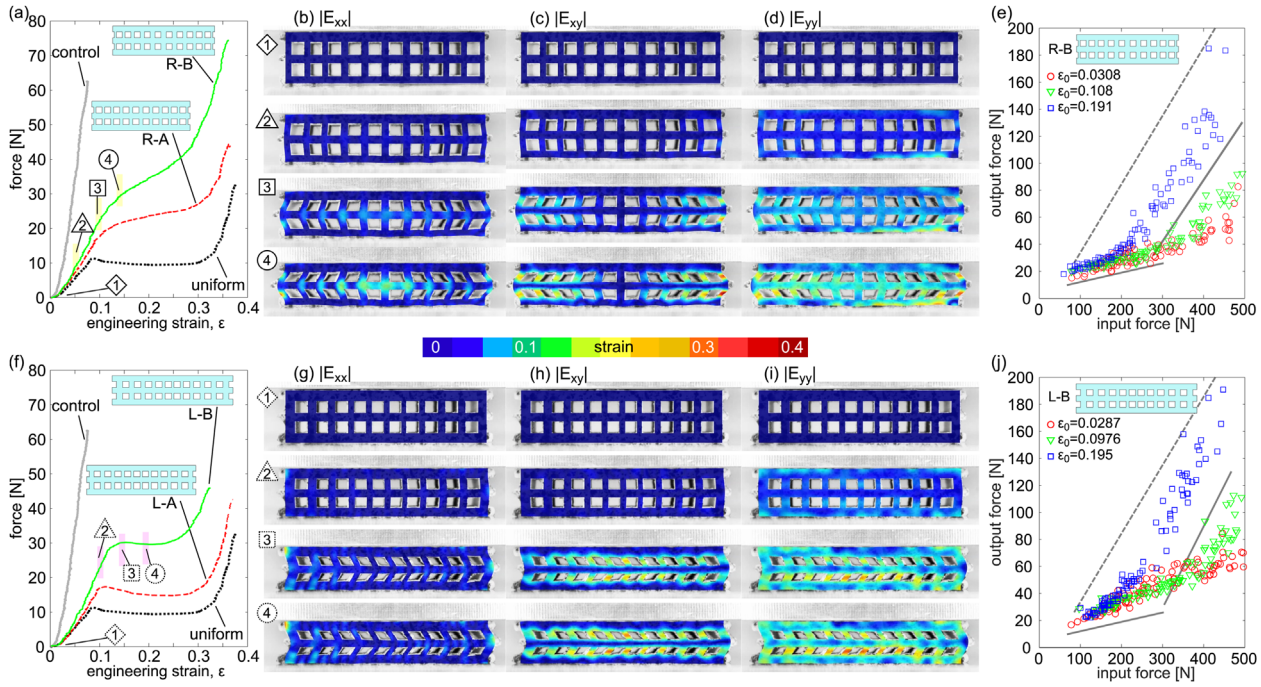

Figure 3. Metamaterials with reprogrammed geometry for tailoring mechanical properties and impact mitigation mechanisms. Force-strain profiles of the R-class metamaterials are given in a), as contrasted with the Uniform and Control specimens. In b–d) are, respectively, $|E_{xx}|$, $|E_{xy}|$, and $|E_{yy}|$ strains of the R-B metamaterial revealing a bimodal deformation with large horizontal beam stretching, suggesting a unique energy dissipation mechanism. In e) are measurements of output force peak as function of input impact force peak for the R-B metamaterial under different pre-strains. Parts f–j) are similar data sets presented for the L-class or L-B metamaterials. In g–i), the L-B is seen to deflect under compression load by unilateral deflection of the horizontal beam such that the vertical beams greatly bend, with more strain in the innermost vertical beams, similar yet distinct compared to the Uniform specimen. The dashed curves in e), j) are the linear fits for the Control, while the solid curves in e), j) are the linear fits for the least pre-strained Uniform metamaterial.

are drastically different compared to the unilateral horizontal beam deflection of the L-B metamaterial that is comparable to the uniform specimen (Figure 3g–i). On the other hand, in contrast to the uniform specimen, the L-B metamaterial induces greater vertical beam shear and vertical strain in the center of the cross-section by virtue of the relative thin-ness of the centermost beam respecting the outer vertical beams (Figure 3h, i). While the R-B specimen likewise shears and vertically strains the vertical beams that buckle (Figure 3c, d), the bimodal buckling causes a unique stretching of the horizontal beam that heightens horizontal normal strain (Figure 3b). As supported by our additional data on the R-A and L-A variants of the metamaterial classes (see Supporting Information for details, and Figure S10), these findings suggest that the reprogrammed geometry of R-class metamaterials couples horizontal beam stretching to the shear and compression of the vertical beams to attenuate input energies that cause vertical deflection of the specimen (Video S4, S8). Such combination of energy dissipation mechanisms does not occur for the L-class metamaterials due to the collective motion of the internal vertical beams (Video S5, S9).

Examining the transmitted output force in the impact experiments reveals that the two, coupled energy dissipation mechanisms of the reprogrammed R-class metamaterials may explain the greater attenuation of the injected energy than the L-class. When least pre-strained, the R-class metamaterials (Figure 3e, S10e) absorb impacts without densification over an increased range of input force than the uniform specimen. Moreover, for the similar vertical beam thickness variation used in the reprogrammed geometries, the R-class reduces the rate of output force increase for the same linear increase of input force, while also minimizing the mean transmitted force when compared to the L-class metamaterials (Figure 3j, S10j, Table S1, S2). The question remains whether these unique mechanisms of internal, reversible elastic energy dissipation observed in the quasistatic loading measurements (Figure 3b–d and g–i, S10b–d, S10g–i) likewise explain the distinctions among the impact energy mitigation characteristics.

Applying our DIC method to impact experiments with the R-B and L-B metamaterials, the anticipation of distinct strain distributions is confirmed. **Figure 4**a–c shows that the R-B specimen undergoes large horizontal beam stretching that is symmetric about a vertical line approximately near to the cross-section center, while vertical beam bending is also apparent. Collectively, the horizontal normal strain, shear, and vertical normal strain are all leveraged by the R-B specimen to suppress the impact force, as observed via results in Figure 3e and Video S6. In contrast to these behaviors, the L-B metamaterial relies largely on vertical normal strain in the vertical beams to attenuate the impact because no significant stretching of the horizontal beam is observed (Figure 4d–f, Video S7). These distinct trends are likewise observed in the R-A and L-A metamaterial variants (Figure S11, Videos S10, S11). Although our DIC method is currently limited by video recording rates, the unprocessed recordings of larger impact experiments confirm that the distinct deformation, and hence microscopic dissipation mechanisms, in the reprogrammed R- and L-class metamaterials persist even to the case of self-contact (Video S12). Despite our current hardware limitation, our total bill of sale of DIC experimental apparatus is less than 5000 USD$ (Table S3), which may considerably broaden the reach of DIC for the scientific communities since this total is more than an order of magnitude less in expense than commercially available DIC packages.

In summary, we have presented a validated approach to DIC that directly illuminates the unique integration of micro- and macroscopic deformations and elastic buckling in elastomeric mechanical metamaterials when subjected to impacts. By reprogramming the internal geometries of vertical beam constituents, we exemplify that impact energy mitigation properties may be made robust to a broad range of shocks and less prone to catastrophic, unilateral buckling. These distinctions of collapse and energy dissipation by reprogramming are aligned with fundamentals of structural engineering.[22] In such contexts, unilateral buckling of built-up frames may be resisted if the vertical columns are resilient enough to bear the applied vertical compressive stress in addition to the shear that is induced by neighboring columns that buckle for less vertical stress.[35] This is clear evidence that mechanical metamaterials are a unique intersection of materials science and structural engineering, and interdisciplinary studies may culminate in innovative concepts for diverse applications. Our experimental methods presented in this report provide researchers tools to correlate intricate deformation behaviors of these metamaterials to the actual energy dissipation mechanisms, a factor that is needed to close the loop that ties together mechanical and dynamic response in the presence of internal instabilities.[17,25] Understanding these energy dissipation mechanisms will propel the potential to translate the concept of mechanical

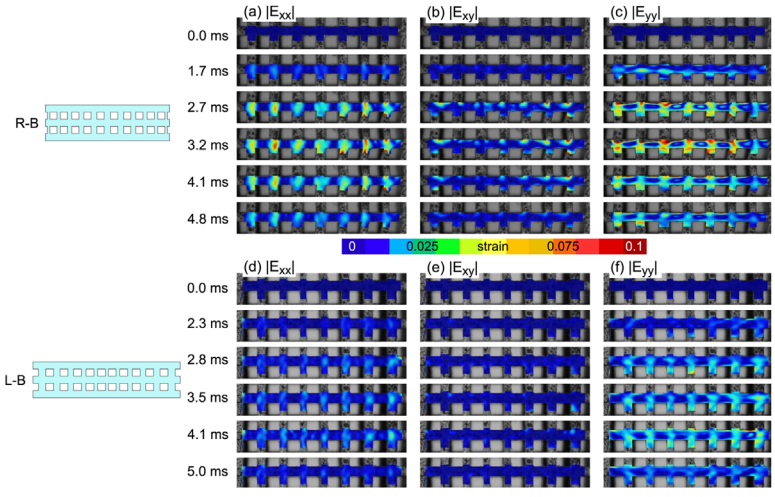

Figure 4. Impact energy dissipation mechanisms in reprogrammed mechanical metamaterials. a–c) show the $|E_{xx}|$, $|E_{xy}|$, and $|E_{yy}|$ strains, respectively, for an impact force of 150 N on the least pre-strained R-B metamaterial. d–f) show the $|E_{xx}|$, $|E_{xy}|$, and $|E_{yy}|$ strains, respectively, for an impact force of 151 N on the least pre-strained L-B metamaterial. The additional impact energy dissipation mechanism enabled by horizontal beam stretching in the R-B metamaterial is confirmed.

metamaterials to applications, including new generations of protective equipment and resilient structures.[16]

Acknowledgements

The authors acknowledge helpful conversations with Dr. Philip R. Buskohl of the Air Force Research Laboratory and Dr. Kazuko Fuchi of the University of Dayton Research Institute in regards to this research. The authors acknowledge the support of Graham Rowan for high-speed camera hardware and software development assistance. This work is supported in part by Owens Corning Science and Technology and in part by the Haythornthwaite Foundation. All authors contributed throughout this research.

Supporting Information

Supporting Information is available online from Wiley Online Library or from the author.

Keywords

Impact, Mechanical metamaterials, Programmable energy dissipation

Received: September 20, 2017
Revised: November 19, 2017
Published online: December 5, 2017

[1] J. J. Crisco, B. J. Wilcox, J. G. Beckwith, J. J. Chu, A. C. Duhaime, S. Rowson, S. M. Duma, A. C. Maerlender, T. W. McAllister, R. M. Greenwald, *J. Biomech*. **2011**, *44*, 2673.
[2] C. Grench, C. Formosa, A. Gatt, *J. Orthopaedics* **2016**, *13*, 148.
[3] L. R. Meza, S. Das, J. R. Greer, *Science* **2014**, *345*, 1322.
[4] S. C. Han, J. K. Lee, K. Kang, *Adv. Mater.* **2015**, *27*, 5506.
[5] L. C. Montemayor, J. R. Greer, *J. Appl. Mech.* **2015**, *82*, 071012.
[6] X. Zheng, W. Smith, J. Jackson, B. Moran, H. Cui, D. Chen, J. Ye, N. Fang, N. Rodriguez, T. Weisgraber, C. M. Spadaccini, *Nat. Mater.* **2016**, *15*, 1100.
[7] T. Frenzel, C. Findeisen, M. Kadic, P. Gumbsch, M. Wegener, *Adv. Mater.* **2016**, *28*, 5865.
[8] D. M. Correa, T. Klatt, S. Cortes, M. Haberman, D. Kovar, C. Seepersad, *Rapid Prototyping J*. **2015**, *21*, 193.
[9] S. Shan, S. H. Kang, J. R. Raney, P. Wang, L. Fang, F. Candido, J. A. Lewis, K. Bertoldi, *Adv. Mater.* **2015**, *27*, 4296.
[10] D. Restrepo, N. D. Mankame, P. D. Zavattieri, *Extreme Mech. Lett*. **2015**, *4*, 52.
[11] J. Bishop, Q. Dai, Y. Song, R. L. Harne, *Adv. Eng. Mater.* **2016**, *18*, 1871.
[12] B. Florijn, C. Coulais, M. Van Hecke, *Phys. Rev. Lett*. **2014**, *113*, 175503.
[13] M. F. Ashby, *Philos. Trans. R. Soc. A* **2006**, *364*, 15.
[14] R. L. Harne, Z. Wu, K. W. Wang, *J. Mech. Des*. **2016**, *138*, 021402.
[15] C. Findeisen, J. Hohe, M. Kadic, P. Gumbsch, *J. Mech. Phys. Solids* **2017**, *102*, 151.
[16] K. Bertoldi, *Ann. Rev. Mater. Res*. **2017**, *47*, 51.
[17] G. Puglisi, L. Truskinovsky, *Continuum Mech. Thermodyn*. **2002**, *14*, 437.
[18] M. Caruel, J. M. Allain, L. Truskinovsky, *Phys. Rev. Lett*. **2013**, *110*, 248103.
[19] I. Benichou, S. Givli, *J. Mech. Phys. Solids* **2013**, *61*, 94.
[20] M. Caruel, J. M. Allain, L. Truskinovsky, *J. Mech. Phys. Solids* **2015**, *76*, 237.
[21] N. Kidambi, R. L. Harne, K. W. Wang, *Smart Mater. Struct*. **2017**, *26*, 085011.
[22] Z. P. Bažant, L. Cedolin, *Stability of Structures: Elastic, Inelastic, Fracture, and Damage Theories*, World Scientific Publishing Co., Hackensack, New Jersey **2010**.
[23] M. Schaeffer, M. Ruzzene, *C. R. Mec*. **2015**, *343*, 670.
[24] R. K. Pal, J. Rimoli, M. Ruzzene, *Smart Mater. Struct*. **2016**, *25*, 054010.
[25] G. Puglisi, L. Truskinovsky, *J. Mech. Phys. Solids* **2002**, *50*, 165.
[26] J. R. Raney, N. Nadkarni, C. Daraio, D. M. Kochmann, J. A. Lewis, K. Bertoldi, *Proc. Natl. Acad. Sci*. **2016**, *113*, 9722.
[27] N. Nadkarni, A. F. Arrieta, C. Chong, D. M. Kochmann, C. Daraio, *Phys. Rev. Lett*. **2016**, *116*, 244501.
[28] M. A. Sutton, J. J. Orteu, H. W. Schreier, *Image Correlation for Shape, Motion and Deformation Measurements: Basic Concepts, Theory and Applications*, Springer, New York **2009**.
[29] P. Reu, *Exp. Techn*. **2012**, *36*, 3.
[30] P. Wang, F. Pierron, M. Rossi, P. Lava, O. T. Thomsen, *Strain* **2015**, *52*, 59.
[31] Y. Wang, A. M. Cuitiño, *Int. J. Solids Struct*. **2002**, *39*, 3777.
[32] M. Schaeffer, G. Trainiti, M. Ruzzene, *Sci. Rep*. **2017**, *7*, 42437.
[33] J. Shim, S. Shan, A. Košmrlj, S. H. Kang, E. R. Chen, J. C. Weaver, K. Bertoldi, *Soft Matter* **2013**, *9*, 8198.
[34] R. L. Harne, D. C. Urbanek, *J. Vibr. Acoust*. **2017**, *139*, 061004.
[35] D. W. White, J. F. Hajjar, *J. Constr. Steel Res*. **1997**, *42*, 171.

Supporting Information

Title: Illuminating origins of impact energy dissipation in mechanical metamaterials

*Peter Vuyk, Shichao Cui, Ryan L. Harne**

1. Materials and Methods

1.1. Metamaterial designs and fabrication

Five metamaterial specimen geometries are investigated in this work. A control specimen composed of the bulk elastomer itself is also studied for sake of comparison to the mechanical and dynamic properties of the metamaterials fabricated using the same elastomer. The dimensions, measures, and design attributes of the metamaterial and control specimens are reported in Table S1. The length spans denoted are the width (horizontal measure of the constant cross-section), the height (vertical measure of the constant cross-section), and depth (extruded dimension of the constant cross-section). The depth length spans of the specimens are more than twice the height spans in which deformation occurs. This accommodation to size helps to enforce the plane strain mode of deformation for the metamaterial specimens due to the internal cellular geometries. Due to the use of the bulk elastomer for the control specimen, the plane strain assumption may not be as well held. On the other hand, the plane strain deformation is practically relevant in this report for sake of the digital image correlation evaluations, in which case the control specimen DIC data does not contribute to the investigations and discoveries of this report. DIC measurements on bulk elastomers are reported in other works [1] [2].

The metamaterial designs considered here consist of a Uniform specimen having uniform thickness vertical beams in the constant cross-section geometry, and R- and L-class designs. The evolution from the Uniform design to the R- or L-class is achieved according to a linear variation of the vertical beam thicknesses in the cross-section cellular geometries. Starting with the vertical beam thickness used for the Uniform specimen, T=0.79 mm, the R-class

metamaterials use this beam thickness on the outermost edges of the cross-section in the horizontal width span. Then, moving towards the center of the specimen, the vertical beam thicknesses are increased in constant amounts that are determined as percents of the T dimension. Thus, the center of the R-class metamaterials utilizes the thickest vertical beam members. Considering a percentage amount of variation denoted as Y%, an R-class metamaterial has outermost vertical beams of thickness T, while the next inner vertical beams have thickness T(1+Y%), then the next inner vertical beams have thickness T(1+2Y%), and so on until the center of the specimen is reached. Here, all metamaterial specimens use 11 vertical beam sets, above and below the middle horizontal beam that guides lateral motion of the metamaterial when it is subjected to vertical load. The L-class metamaterials are designed in the opposite way as the R-class. In other words, for L-class metamaterials the thickest vertical beams are the outermost of the cross-section geometry, while the center beam is the thinnest at dimension T. These aspects are summarized in Table S1.

The process of metamaterial specimen fabrication begins with the design of mold geometries that are the negatives of the elastomer elements aimed to be fabricated. The mold geometries are composed of two components, a base and a shell, whose forms are realized in computed aided design (CAD) software. A FlashForge Creator Pro 3D printer is utilized for mold printing of STL files output from the CAD models. After the printed mold components have cooled to room temperature, Figure S1, they are assembled by setting the shell onto the base using wax that seals the two components into a working mold, Figure S2. The coupled components are then filled with Smooth On, Inc., Mold Star 15S silicone rubber that is mixed from its two-part base materials. After curing for 24 hours, the mold components are disassembled by removing the wax seal. This allows the metamaterial specimen to be removed from the mold with relative ease, and also enables the reusability of the molds.

Specimens are cleaned with cold water and allowed to sit for >72 hours before use in experimentation.

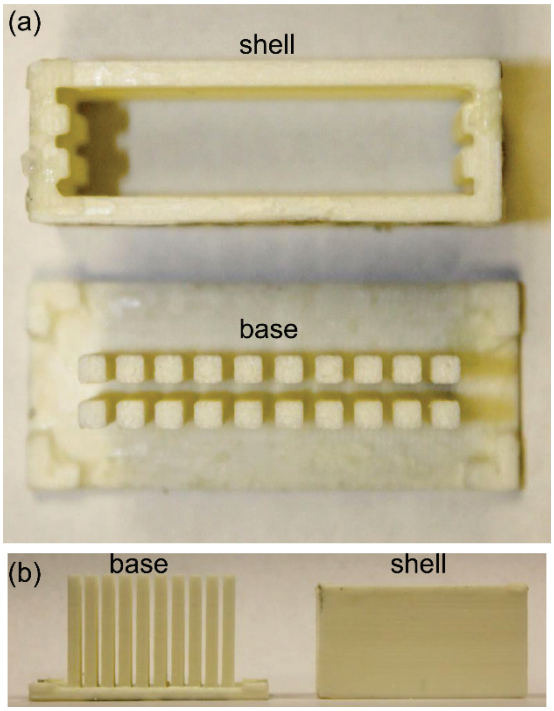

Figure S1. Base and shell components of the 3D printed mold for a metamaterial specimen with uniform beam thicknesses as fabricated. Mold components are shown in (a) top view and (b) side view.

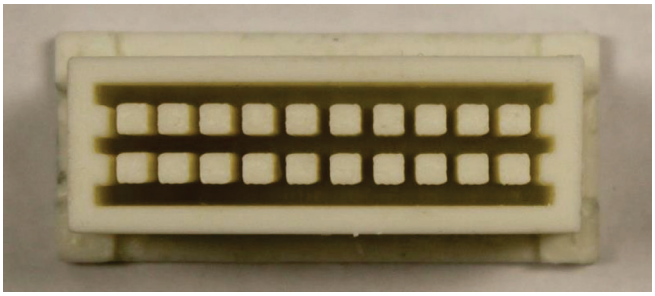

Figure S2. Top view of assembled mold whose two individual components are shown in Fig. S1.

2. Finite element modeling of quasistatic response

The finite element (FE) software COMSOL Multiphysics is used to predict the quasistatic force-displacement profile of the metamaterial with uniform thickness beams in the cross-section.

In the plane strain FE model, the elastomeric metamaterial geometry is modeled in accordance with the size of the "Uniform" experimental specimen, which has uniform beam thicknesses throughout the constant cross-section, as described in Table S1. The FE mesh is shown in Figure S3. The quadrilateral mesh density is determined following a mesh convergence study that identified a suitably refined mesh that leads to consistent results without excessive computation time. The FE model accounts for vertical displacement to the topmost boundary of the specimen. Lateral motions of the top horizontal beam member is inhibited, which is observed to improve computational stability for post-buckling response and is similar to the quasistatic loading experimentation, Sec. 3. The bottom boundary of the metamaterial specimen geometry is prevented from displacing, similar to the experimental setup, Sec. 3.

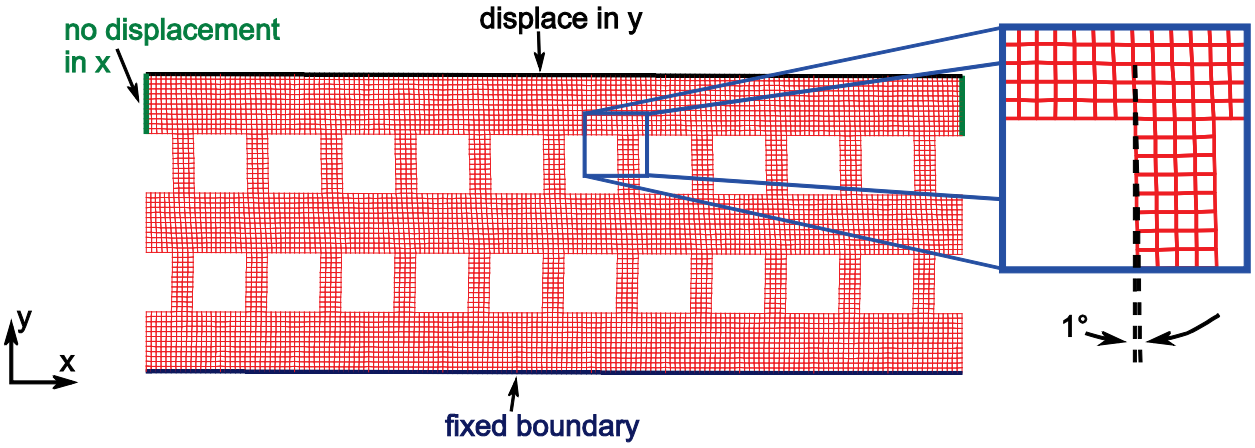

Figure S3. FE mesh, boundary conditions, and use of imperfectly vertical beams to induce buckling.

Another effort to improve the ability of the FE model to characterize the post-buckling response is to use geometries that are slightly imperfect respecting an ideal internal structure of vertical, arrayed beams. Therefore, in the FE model, the vertical beams are rotated by 1° so as to induce the lateral motion of the specimen observed experimentally. In the specimen fabrication, tolerances are such that deviations on this order are possible, which provides a rationale basis for such incorporation of imperfection in the FE model. Such accommodation

to practical imperfections enables the FE model to predict the post-buckling deflections of the metamaterial. It is found that the computations cannot proceed beyond the bifurcation point where buckling occurs without this feature built in to the geometry. On the other hand, with this accommodation, a significant portion of the post-buckling response can be accurately predicted respecting the measurements, Figure 1a, almost to the point of self-contact. Self-contact is not able to be characterized in the current FE code.

A hyperelastic material model is used to study the silicone rubber in the FE simulations. A Neo-Hookean formulation of the strain energy is employed, with the following material properties: Young's modulus E 752 kPa, Poisson's ratio ν 0.49, density ρ 1,145 kg/m^3, Lame parameter λ 12.36 MPa, and Lame parameter μ 252.3 kPa. The Young's modulus and density are determined empirically from the silicone rubber, while the Poisson's ratio is assumed based on common knowledge of nearly incompressible elastomers, and the Lame parameters are derived from the prior material properties.

By comparison with experimental measurements using the DIC method in Figure 1c,d,e showing the agreement between FE predictions and experimental data, we verify the efficacy of the experimental approach to be used for further study of the impact response. This contrasts with extending the FE model to characterize shock or impact loading of the metamaterials. The impact response of the metamaterials is more challenging and time-consuming to compute by FE software due to the large strains, nonlinearities, and instabilities involved [3] [4] [5] [6], when compared to the time taken for experimental characterization.

3. Experimental mechanical properties characterization

A load frame (Mark-10 ES20) experimental setup is utilized to determine the mechanical properties of each specimen when subjected to uniaxial compression in the height dimension. A load cell (PCB 110205A) and signal conditioner (PCB 8162011A) are used for measuring the uniaxial force on the specimens as an aluminum platen is brought down on the top of each

specimen which rests on a fixed aluminum platen, as shown in Figure S4. A laser displacement sensor (Micro Epsilon ILD1700) monitors the corresponding one-dimensional motion of the top, moving aluminum platen. Prior to collecting data, the specimens are exercised via cycles of loading and unloading to ensure that the specimens are situated in equilibrium respecting their position on the fixed aluminum platen. Then, with a strain rate of 0.002 strain/s, the measurements are acquired of the uniaxial force and displacement at a sampling rate of 256 Hz. The data are digitally filtered with a low pass filter at 35 Hz prior to data display in this report.

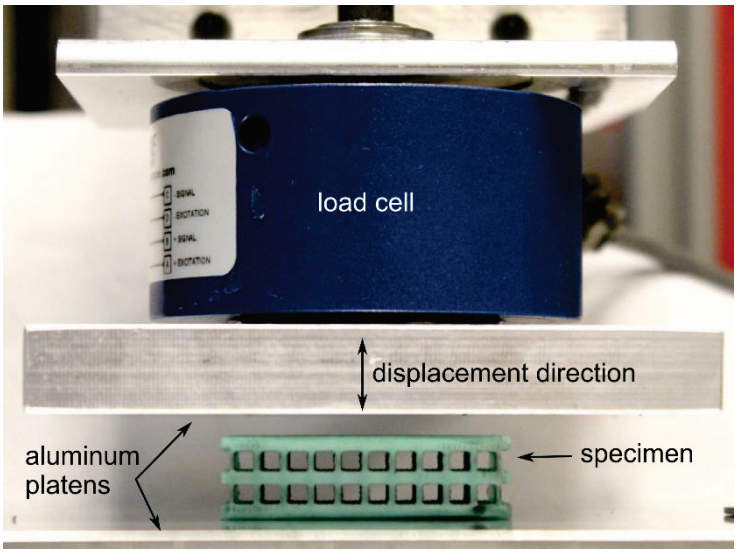

Figure S4. Experimental setup to characterize mechanical properties of the specimens.

The one-dimensional stiffness, around a given displacement, is assessed according to the slope of the curves shown in Figure 1a and Figure 3a,f. For the metamaterial specimens that undergo unilateral elastic buckling when subjected to quasistatic or impact load, a region of negative stiffness is observed following a local maxima of the force in the quasistatic load frame measurements. Specifically, the Uniform and L-class metamaterials exhibit such local maxima followed negative stiffness regions as seen in Figure 3f around the engineering strain ε range of 0.08 to about 0.14. In contrast, no such negative stiffness occurs for the R-class metamaterials since the load frame measurements, shown in Figure 3a, do not exhibit local

maxima. Instead, a softening of the one-dimensional stiffness is induced for the R-class metamaterials, as evidenced by the shallower (yet never negative) slopes of the R-A and R-B curves in Figure 3a in the strain range around 0.1 to 0.28.

4. Experimental characterization of impact response

Impact experiments are undertaken to characterize the capabilities of the metamaterial and control specimens to mitigate shock energies. To investigate the role of the pre-strain ε_0 on specimens prior to the delivery of the impacts, which is comparable to bearing an initial static load, the specimens are placed into a fixture that enables a tuning of the initial strain state. As seen in Figure S5, each specimen is placed on a bottom aluminum plate with platform area considerably greater than the resting surface area of the bottom of the specimen. A top aluminum plate variably constrains the specimen to the bottom plate via polyethylene lines, whose tension is set according to a force tuner. In practice, the plates are tightened down via the force tuner and the pre-strain ε_0 is set by measuring the distance between the two plates at all four corners where the lines make contact from the top to bottom plates. In this way, a state of initial pre-strain ε_0, or alternatively a static compressive force, is set via the fixture.

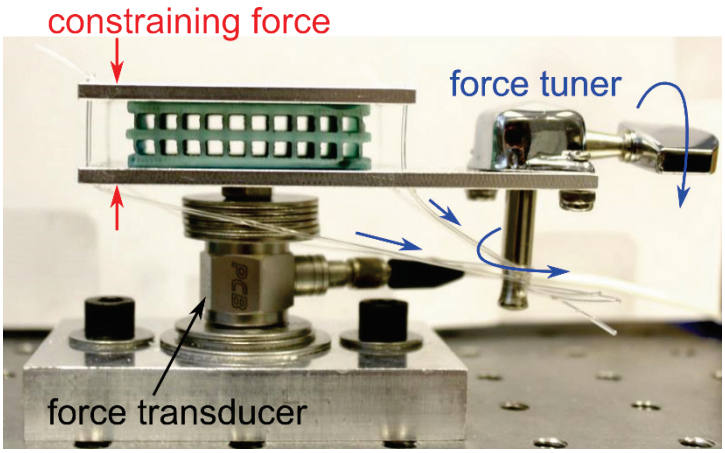

Figure S5. Experimental setup for characterizing impact force transmission through the specimens. Specimens are affixed between two aluminum plates via polyethylene lines attached to a force tuner. The bottom of the aluminum plates is connected to an output force transducer. The impact is delivered by an impact force transducer hammer on the topmost aluminum plate shown here.

Impacts are applied with an impact modal hammer (PCB 086C03) to the topmost aluminum plate, Figure 2a. The modal hammer includes a force transducer on its working end. Based on the hammer mass and aluminum hammer tip, broadband frequency energy is imparted to the specimens. The output force transmitted through the specimen is measured by a force transducer (PCB 208C03). These force transducers are matched in sensitivity range to maximize the quality of the measured data. In the experiments, the experimentalist uses the modal hammer to strike the center of the top plate in a line of action parallel to the axis of motion of the specimen, which minimizes off-axis components of the imparted force. This uniaxial impact event is comparable to the impact imparted to a specimen in drop experiments [7]. A range of input force amplitudes around 50 N to 500 N is considered in this work due to the capability of this force range to probe the full dynamic regimes of impact mitigation behavior provided by the metamaterial and control specimens. The polyethylene lines are regularly replaced in the experimental sequence to ensure that consistent pre-strain is applied from one specimen to the next, due to the gradual wear of the lines according to the relative motion of the plates during impacts. Data is acquired at 131 kHz from the input and output force transducers. This data sampling rate is observed to adequately capture the impact events in full detail. Prior to using the measurements acquired from the impact experiments, the data is digitally filtered with a bandpass filter from 50 to 18k Hz.

In the experiments, the tunable constraint is applied only at a mild level for the control specimen due to difficulty in applying great compression to the bulk elastomer. For the Uniform metamaterial, large influence of tuning the constraint near pre-strain ε_0 around 0.03 to 0.04 is observed towards tailoring the output transmitted force as a function of the input force amplitude. Little influence is observed in tuning the constraint for the Uniform metamaterial in the range of around 0.11 to 0.20 pre-strain ε_0. Collectively, this explains the presentation of results in Figure 2b of the main text that gives measurements for the cases of

pre-strain 0.0326, 0.0436, and 0.194. For the R- and L-class metamaterial specimens, unique trends in the measurements are obtained in the pre-strain regimes of 0.03-0.05, 0.09-0.11, and 0.19-0.21, which are sufficiently pre-, near-, and post-buckling according to the load-displacement measurements respectively given in Figure 3a and f.

5. Digital image correlation methods and data processing

The digital image correlation (DIC) method of data capture and visualization is enhanced in this research in order to empower ability to probe the deformation and energy dissipation mechanisms in mechanical metamaterials composed of elastomers.

5.1. DIC specimen preparation

The metamaterial and control specimens are prepared with a speckle pattern prior to their use in the DIC-based experiments. A charcoal microparticle powder (BOS Essential Activated Charcoal Powder) is found to supply sufficient contrast with the light green surface of the silicone rubber elastomer. Based on the pigment of the specific elastomer used, different speckling approaches may be employed, including talc powder [1] and ceramic particles in an adhesive spray [2]. In this study, the microparticles of charcoal are found to be well-suited to adhering to the silicone rubber elastomer while the size of the particles is found to be conducive to obtaining repeatable and accurate DIC processed data from the video recordings due to sufficiently small speckles available in each subset of pixels used for correlation.

As shown in Figure S6, the charcoal is applied to a clean glass microscope slide, and distributed in a random way that maintains relatively consistent speckle density across the slide area.

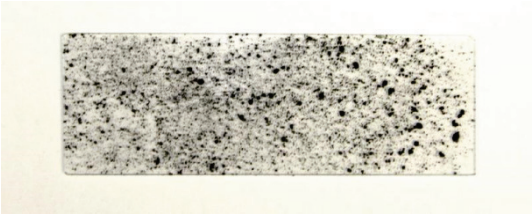

Figure S6. Glass slide with charcoal powder used to create speckle pattern.

After the specimens are prepared by the molding strategy described in Sec. 1, the speckle pattern is applied to the specimen cross-section by gently depressing the specimen cross-section face to the glass slide. The specimen is then removed from the slide without sliding it relative to the slide surface, to inhibit development of smudging of charcoal powder particles. The outcome of this process is seen in Figure S7.

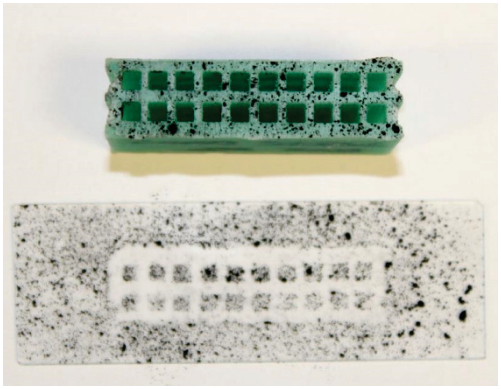

Figure S7. Outcome of depressing metamaterial specimen to the glass slide, showing the adherence of the charcoal to the elastomer.

5.2. Frame capture for quasistatic and impact measurements

To capture the high-speed video recordings of the specimens as prepared with the speckle pattern, the DIC hardware includes a high-speed video camera (The Slow Motion Camera Company fps1000HD) with lens (Canon EF-S 18-55mm f/3.5-5.6 IS II) and LED lights (Neweer CN-216) to provide sufficient brightness required for DIC data post-processing at the high frame rates of the video capture. A trigger is used to control the camera shutter so that synchrony is obtained between video collection and the quasistatic loading or moments of impact. In all experiments for the DIC evaluations, a white background is placed behind the specimen to enhance contrast between the specimen and backward for sake of the data post-processing [8]. The experimental setup for high-speed video capture in the impact experiments is shown in Figure S8.

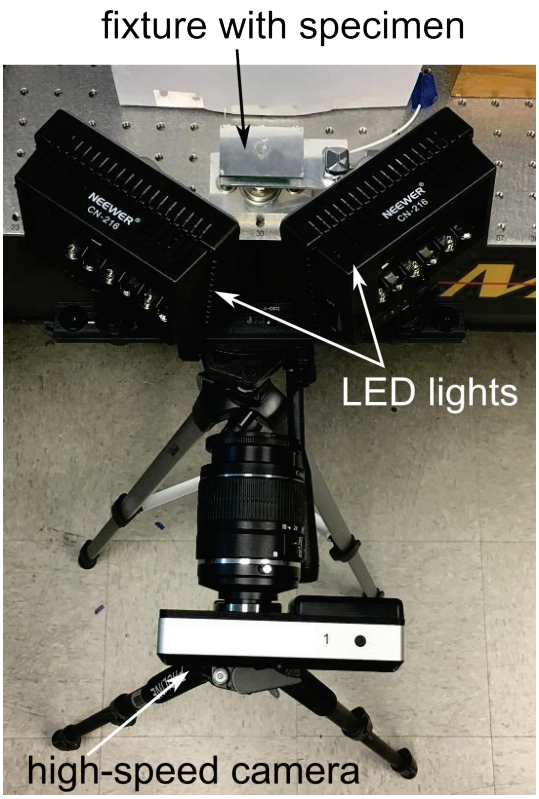

Figure S8. Experimental setup with high-speed camera and LED lights to capture the impact deformation of the metamaterial and control specimens.

For quasistatic evaluations in the load frame, the video record rate is 1,000 frames per second over a video frame area of 1280 pixels x 720 pixels. This frame area is sufficient to observe the entire material system specimen. For the impact experiments, the video record rate is 10,000 frames per second over a video frame area of 640 pixels x 120 pixels. This frame area is zoomed in to observe 7 of the 11 vertical beams in a given material system specimen. This leads to a frame area of approximately 65 pixels x 30 pixels to characterize the displacement and strain of a given vertical beam segment. With the ample contrast of the light green elastomer and deep black of the charcoal powder microparticles, a sufficient convergence of DIC results is obtained for both quasistatic load frame and impact evaluations. The process of speckling and measuring specimens under these experimental conditions is repeated until the speckling process is found to yield consistent DIC post-processed displacements and strains. The agreement to the finite element simulations, Fig. 1c-e, also supports the experimental method undertaken to obtain the convergent displacement and strain DIC data. To have

comparison of DIC results across the range of specimens studied in this report, all cases of DIC data processed for impact evaluations are examined for impact input forces with amplitudes around 150 N. The specific range is from 148 N to 156 N of impact force.

5.3. DIC data post-processing and results

The software used to post-process the high-speed video recordings is a 2D DIC code developed at the University of Illinois at Urbana-Champaign, and made available to the public [9]. The DNG image files obtained from the high-speed video camera are converted to an uncompressed format and then cropped prior to use in the DIC code. Due to the large deformations and short time scales involved, an appreciable padding of pixels around the data points is required where displacement and strain are computed, with greater such padding demanded when these factors are amplified, as in the impact measurements. This explains why the padding around the DIC data from quasistatic measurements from the load frame evaluations is negligible respecting the whole working area of the specimens under the load, when compared to the more significant padding observed in the DIC data collected and processed from the impact measurements. Bi-cubic finite element shape functions are used in the displacement and strain interpolation procedures. Subset sizes for the measurements are consistently around 31 pixels, and each subset contains around 4 to 8 speckles from the microparticle charcoal powder treatment to the specimens. To improve the DIC data post-processing according to the large deformations observed in this research, a serial-based image referencing approach is used from one correlation step to the next so that each subsequent correlation uses the prior image for referencing.

6. Supporting experimental results

6.1. Representative impact response

Figure S9 presents representative time series of impacts delivered and measured by the force transducers. Each part of Figure S9 shows a representative snap shot for a different specimen. Several aspects of the results are worth assessing.

The input impact force shows a clear peak shortly after it impacts the top plate. This is the force amplitude value that is plotted in Figure 2b, Figure 3e,j, and Figure S10e,j. The output force then begins to increase and reaches a peak value, typically 2 to 3 ms after impact for the metamaterial specimens and approximately 1.5 ms after impact for the control specimen. These time spans are comparable to the DIC snap shots, shown in Figure 2c,d,e, Figure 4, and Figure S11, to conclude that the peak transmitted force occurs when the internal metamaterial beam structures are most greatly strained.

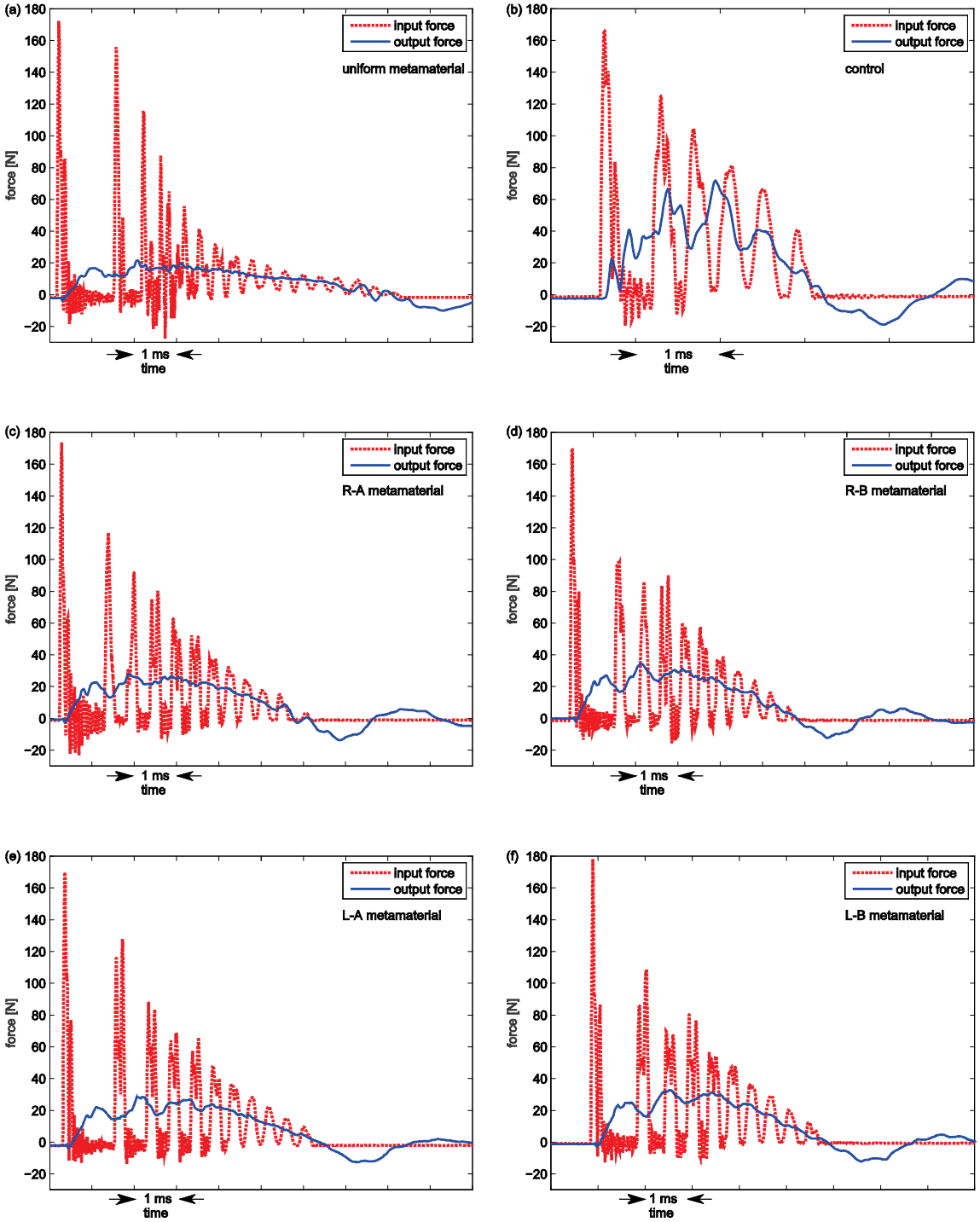

Figure S9. Representative time series of the impact response of the specimens. Input and output force responses are shown, where the input force is delivered by the impact hammer and the output force is measured below the specimen in the fixture, see Figure S5. Here, the results are shown for (a) uniform metamaterial, (b) control specimen, (c) R-A metamaterial, (d) R-B metamaterial, (e) L-A metamaterial, and (f) L-B metamaterial.

It is observed in Figure S9 that the input impact force is not a single half-sine or shock profile.

Based on the sound speed in the elastomer $c = \sqrt{\frac{E(1-\nu)}{\rho(1+\nu)(1-2\nu)}}$, approximated to be around

100 m/s using the material properties identified in Sec. 2, a bulk wave will travel back and forth through the 12 mm tall specimens in approximately 0.25 ms. In the time series, the multiple peaks observed after the initial impact force are observed to be spaced by approximately 0.3 ms. This suggests that the multiple input force peaks, albeit diminishing as time elapses, are associated with reflections of the initial impact transmitting back and forth through the specimens that subsequently reach the force transducer on the tip of the impact hammer, thus registering as "input force". Consequently, for the realistic case of impact considered here by a hammer input respecting the dimensions of the specimen, the impact hammer is not able to be removed from the specimen following the initial impulse delivered in brief enough time to prevent the measuring of multiple "input force peaks". On the other hand, based on the calculations and values identified here, the actual impulse delivered to the specimens is the first peak shown in the time series examples of Figure S9, while the remaining peaks are associated with wave reflections that impinge on the input impact hammer force transducer. Although this study does not impart a perfect half-sine or shock profile to the specimens, there are diverse methods and conventions used in the study of impact or blast mitigation materials and structures [10] [11] [12] [13] [14] so that the selection of one approach is subject to preference and research need.

6.2. Characterization of mechanical properties and impact mitigation in R-A and L-A metamaterials

Figure S10 presents the compilation of results for the load frame measurements to characterize the mechanical properties and the impact measurements to assess transmitted force suppression in the metamaterials R-A and L-A.

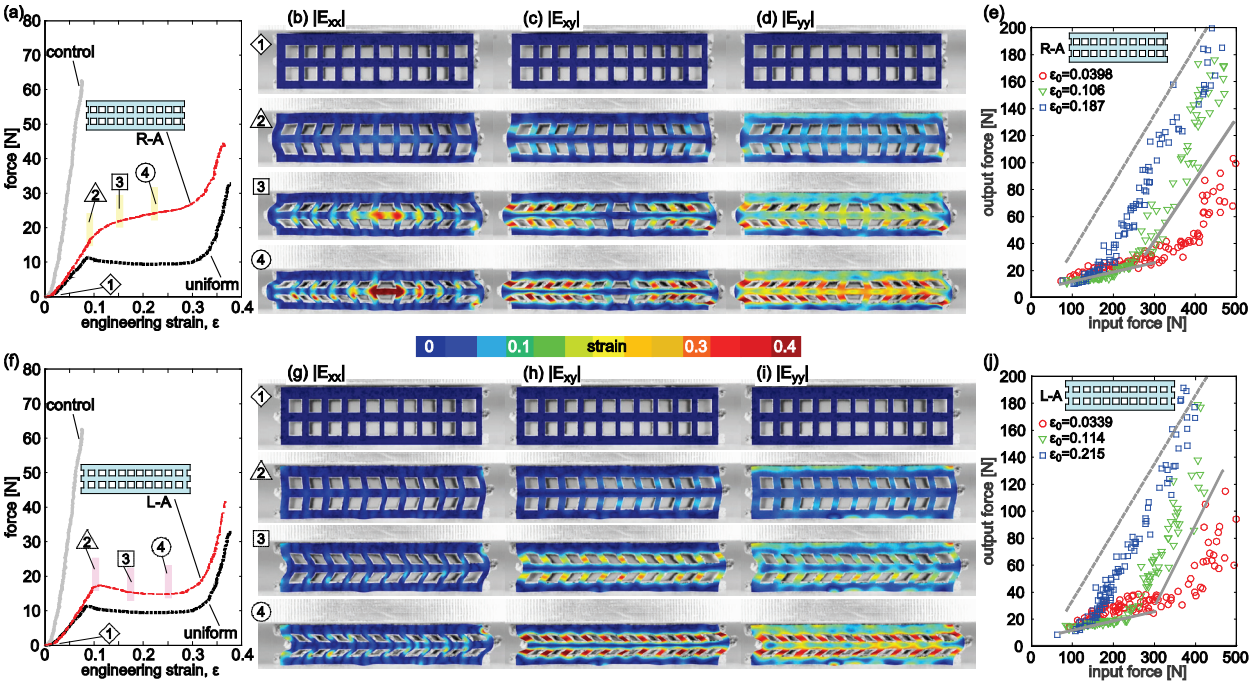

Figure S10. Force-strain profiles of the R-A metamaterial is given in (a), as contrasted with the Uniform and Control specimens. In (b), (c), and (d) are respectively $|E_{xx}|$, $|E_{xy}|$, and $|E_{yy}|$ strains of the R-A metamaterial, showing the increased horizontal beam stretching that results from a bimodal lateral deflection of the horizontal beam according to the different directions of vertical beam buckling, similar to the R-A metamaterial. In (e) are measurements of output force peak as function of input impact force peak for the R-A metamaterial under different pre-strains. Parts (f,g,h,i,j) are similar data sets presented for the L-A metamaterial. The predominant vertical beam bending, with increased bending in the center of the cross-section geometry that is observed in (g) is similar to the measurements for the L-B metamaterial. The dashed curves in (e,j) are the linear fits for the Control, while the solid curves in (e,j) are the linear fits for the least pre-strained Uniform metamaterial.

The R-A and L-A specimens exhibit mechanical properties with force-strain relationships that are an intermediate step from the Uniform metamaterials to their respective B-type variants, Figure 3a,f and Figure S10a,f. A similar observation is made via the impact measurements of output to input force amplitudes in Figure S10e,j for R-A and L-A, respectively, when compared to their counterparts R-B and L-B, respectively, whose data are shown in Figure 3e,j.

The DIC data for R-A and L-A metamaterials, Figure S10b-d and g-i, likewise reveal trends that respectively blend characteristics of the R-B and Uniform or L-B and Uniform metamaterial specimens. For instance, the R-A DIC data in Figure S10b-d shows the bimodal

lateral deformations also observed for the R-B metamaterial. Yet, rather than splitting in lateral deformation trend in a mirror symmetric way like the R-B metamaterial Figure 3b-d, the R-A metamaterial has an asymmetric deformation with the transition of the deformation phase occurring off-center Figure S10b-d. The increased horizontal normal strain consequently follows the inflection of the lateral horizontal beam deflection, Figure S10b. Like the L-B specimen, the L-A metamaterial shows increased shear strain on the innermost vertical beam, Figure S10h labels 2, 3. On the other hand, when the L-A metamaterial is compressed more greatly as shown in Figure S10g-i label 4, the deformation trend is more analogous to the results for the Uniform metamaterial. Consequently, in these ways, the R-A and L-A metamaterials reveal that the design parameter of linear variation of the vertical beam thickness from outer to center beams is a direct way to reprogram the deformation modes, and hence energy dissipation mechanisms, of the mechanical metamaterials.

6.3. DIC data for R-A and L-A metamaterials when subjected to impact forces

Figure S11 presents representative DIC data for 150 N impact forces applied to the metamaterials R-A and L-A. Figure S11a-c provides the results for displacement and strain, respectively, for R-A, while Figure S11d-f provides results of displacement and strain, respectively, for L-A.

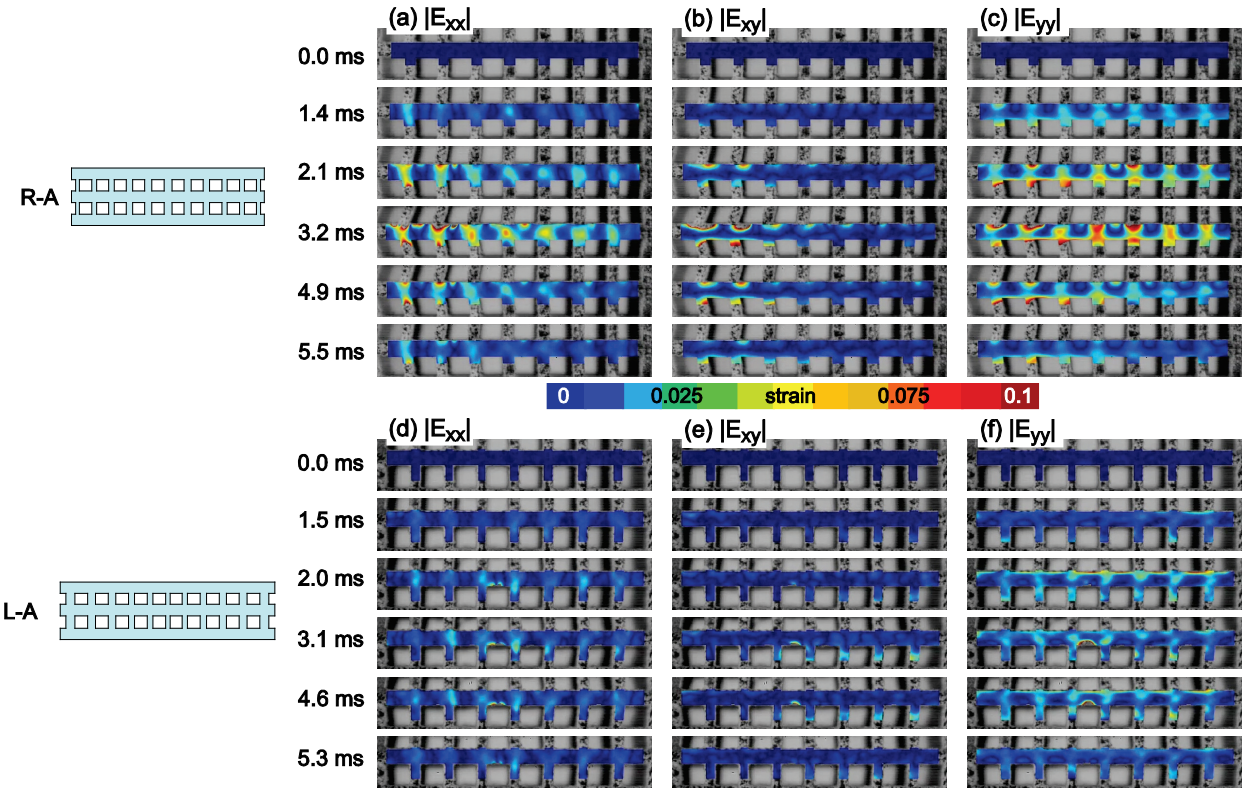

Figure S11. (a), (b), and (c) show the $|E_{xx}|$, $|E_{xy}|$, and $|E_{yy}|$ strains, respectively, for an impact force of 150 N on the least pre-strained R-A metamaterial. (d), (e), and (f) show the $|E_{xx}|$, $|E_{xy}|$, and $|E_{yy}|$ strains, respectively, for an impact force of 151 N on the least pre-strained L-A metamaterial. In these results, the R-A metamaterial reveals greater horizontal beam stretching in the strain profile while the L-A specimen undergoes a greater proportion of vertical beam strain and especially bending. Together, these findings support the conclusions of the main text regarding the ability to program the impact energy dissipation mechanism effectiveness via the relative thickness of the metamaterial internal vertical beam geometry.

The results of Figure S11 support the conclusions drawn in the main text. In particular, the R-A metamaterial deforms with a characteristic bimodal way such that the vertical beams deflect laterally away from the center beam, whereas the deformation of the L-A metamaterial exemplifies a unilateral deflection of the vertical beams. These aspects are in agreement with trends observed for the quasistatic measurements of the respective R- and L-class metamaterials, shown in Figure 3b-d and g-i and Figure S10b-d and g-i. In addition, the strain distributions seen in Figure S11 for R-A and L-A likewise reveal that the R-A undergoes a considerably greater proportion of horizontal beam stretching, and horizontal normal strain

$|E_{xx}|$, than the L-A metamaterial. The L-A metamaterial instead shows that most energy dissipation is in the vertical beam structures as they are subjected to vertical normal strain.

These nuances captured via the DIC data explain results in the synthesized output to input force data seen in Figure S10e,j. For the R-A metamaterial under the least pre-strain (3.98%, red circle data points), a linear curve fit of the output force to input force trends in Figure S10e from 50 to 400 N input force indicates that the output force is $f_{out} = 0.0839 f_{in} + 6.51$ N, such that the mean output force in this input force range is 21.2 N. The least pre-strained L-A metamaterial data in Figure S10j yields a linear curve fit over the same input force range is $f_{out} = 0.0849 f_{in} + 8.94$ N such that the mean output force in this input force range is 23.8 N.

The linear curve fits are contrasted to the other metamaterials and baselines in Table S2. Based on these linear fits and in agreement with trends observed contrasting R-B and L-B metamaterials in the respective output to input impact force transmission behaviors in Figure 3e,j, the R-A metamaterial results in a reduced linear increase of output force for linear increase in input force and less mean transmitted force over the range of 50 to 400 N when compared to the L-A metamaterial. The findings directly support the conclusions of the main text regarding distinctions between the R- and L-class metamaterials, as elucidated by the specific energy dissipation mechanisms involved.

Table S1. Dimensions, measures, and design attributes of the metamaterial and control specimen geometries. The baseline dimension T is 0.79 mm, which is the thickness of the vertical beams used in the Uniform specimen.

Specimen	**Mass [g]**	**Width [mm]**	**Height [mm]**	**Depth [mm]**	**Description**
Control	16.48	49.03	12.00	25.04	Solid elastomer
Uniform	10.03	42.06	12.13	26.18	All vertical beams have thickness T
R-A	10.77	45.04	12.12	26.26	Beam thicknesses increase from outer to center beams by the constant amount 6% T
R-B	11.66	47.86	12.12	26.18	Beam thicknesses increase from outer to center beams by the constant amount 24% T
L-A	10.64	44.88	12.15	26.16	Beam thicknesses increase from center to outer beams by the constant amount 6% T
L-B	12.28	48.15	12.07	26.21	Beam thicknesses increase from center to outer beams by the constant amount 24% T

Table S2. Linear curve fits of impact measurements. The coefficients indicated follow an equation form $f_{out} = m f_{in} + n$. In the cases of the metamaterials, the fits use the impact measurements for the least pre-strained specimens.

Specimen (input force fit range)	m **[N/N]**	n **[N]**	**mean output force peak at 175 [N] input force**
Control (50-400 N)	0.506	-16.8	n/a
Uniform (50-300 N)	0.0690	5.32	17.4
Uniform (300-450 N)	0.604	-152	n/a
R-A (50-400 N)	0.0839	6.51	21.2
R-B (50-400 N)	0.0844	11.0	25.8
L-A (50-400 N)	0.0849	8.94	23.8
L-B (50-400N)	0.149	4.93	31.0

Table S3. Approximate bill of sale of experimental apparatus used to undertake the DIC measurements.

Apparatus	**Approximate Cost [USD$]**
High-speed video camera	2,500.00
LED lights	70.00
Camera remote switch	10.00
Tripods	30.00
Metamaterial constraining fixture	50.00
Force transducers incoming/outgoing	1500.00
MATLAB 2D-DIC code	N/A, [9]
Total	$4,160.00

References

[1] J. de Crevoisier, G. Besnard, Y. Merckel, H. Zhang, F. Vion-Loisel, J. Caillard, D. Berghezan, C. Creton, J. Diani, M. Brieu, F. Hild, S. Roux, *Polymer Testing* **2012**, *31*, 663-670.

[2] T.I. Lee, M.S. Kim, T.S. Kim, *Polymer Testing* **2016**, *51*, 181-189.

[3] L. Gong, S. Kyriakides, *International Journal of Solids and Structures* **2005**, *42*, 1381-1399.

[4] Y.A. Bahei-El-Din, G.J. Dvorak, O.J. Fredericksen, *International Journal of Solids and Structures* **2006**, *43*, 7644-7658.

[5] M. Grujicic, W.C. Bell, B. Pandurangan, T. He, *Materials and Design* **2010**, *4050-4065*(31),.

[6] I. Karen, M. Yazici, A. Shukla, *Composite Structures* **2016**, *158*, 72-82.

[7] J. Bishop, Q. Dai, Y. Song, R.L. Harne, *Advanced Engineering Materials* **2016**, *18*, 1871-1876.

[8] M. Schaeffer, G. Trainiti, M. Ruzzene, *Scientific Reports* **2017**, *7*, 42437.

[9] E.M.C. Jones, Ö.Ö. Çapraz, S.R. White, N.R. Sottos, *Journal of The Electrochemical Society* **2016**, *163*, A1965-A1974.

[10] A. Shukla, Y.D.S. Rajapakse, M.E. Hynes, editors, *Blast Mitigation: Experimental and Numerical Studies*, Springer, New York, **2014**.

[11] D.E. Krzeminski, J.T. Goetz, A.P. Janisse, N.M. Lippa, T.E. Gould, J.W. Rawlins, S.G. Piland, *Sports Technology* **2011**, *4*, 65-76.

[12] C.Y. Zhou, T.X. Yu, R.S.W. Lee, *International Journal of Mechanical Sciences* **2008**, *50*, 905-917.

[13] P.A. Du Bois, S. Kolling, M. Koesters, T. Frank, *International Journal of Impact Engineering* **2006**, *32*, 725-740.

[14] K.S. Shain, M.L. Madigan, S. Rowson, J. Bisplinghoff, S.M. Duma, *Clinical Journal of Sports Medicine* **2010**, *20*, 422-427.

Descriptions of video files

Video S1. The Uniform metamaterial is fixtured in the impact force measurement apparatus and imparted with an impulsive force from the hammer with an input force amplitude around 200 N. Playback of the same impact is given at 1/1, 1/2, 1/4, and finally 1/400 of the real-time speed to appreciate the time scales at which the energy dissipation phenomena involved occur.

Video S2. The Uniform metamaterial is compressed in the load frame. The DIC speckle pattern is applied to the metamaterial for sake of the video capture and DIC data post-processing. The top left quadrant of the video is the unprocessed video images. The top right, bottom left, and bottom right quadrants of the video are the magnitudes of the shear strain $|E_{xy}|$, horizontal normal strain $|E_{xx}|$, and vertical normal strain $|E_{yy}|$, respectively, determined from the DIC post-processing. The video is played back at a rate of 1 s for 450 ms of real-time. The unilateral deflection of the horizontal beam and hence more uniform vertical beam bending trends are observed in the full field strain data of the DIC output. These deformations are anticipated to correspond to the dynamic energy dissipation mechanisms leveraged by the metamaterial when subjected to impact energy.

Video S3. The Uniform metamaterial is subjected to an impact of 148 N on the top surface. The high-speed video capture gives attention to both the middle horizontal beam and the bottommost layer of vertical beams in the metamaterial cross-section to characterize the strain field. The top left quadrant of the video is the unprocessed video images. The top right, bottom left, and bottom right quadrants of the video are the magnitudes of the shear strain $|E_{xy}|$, horizontal normal strain $|E_{xx}|$, and vertical normal strain $|E_{yy}|$, respectively, determined from the DIC post-processing. The video is first played back at 1 s for 10 ms of real-time in two sequences, and then played back at a rate of 1 s for 0.5 ms of real-time. The vertical beam bending and induced strain are evident in the bottom portion of the video, exemplifying the primary mechanism of energy dissipation for this class of metamaterial geometry.

Video S4. The R-B metamaterial is compressed in the load frame. The DIC speckle pattern is applied to the metamaterial for sake of the video capture and DIC data post-processing. The top left quadrant of the video is the unprocessed video images. The top right, bottom left, and bottom right quadrants of the video are the magnitudes of the shear strain $|E_{xy}|$, horizontal normal strain $|E_{xx}|$, and vertical normal strain $|E_{yy}|$, respectively, determined from the DIC post-processing. The video is played back at a rate of 1 s for 450 ms of real-time. The bimodal deflection of the horizontal beam and hence greater stretching of the horizontal beam (than the Uniform and L-class metamaterials) are observed in the full field strain data of the DIC output. In addition to this, the vertical beams undergo bending as they deflect in their respective directions considering the mostly unmoving center vertical beam. These deformations are anticipated to correspond to the dynamic energy dissipation mechanisms leveraged by the metamaterial when subjected to impact energy.

Video S5. The L-B metamaterial is compressed in the load frame. The DIC speckle pattern is applied to the metamaterial for sake of the video capture and DIC data post-processing. The top left quadrant of the video is the unprocessed video images. The top right, bottom left, and bottom right quadrants of the video are the magnitudes of the shear strain $|E_{xy}|$, horizontal normal strain $|E_{xx}|$, and vertical normal strain $|E_{yy}|$, respectively, determined from the DIC post-processing. The video is played back at a rate of 1 s for 450 ms of real-time. The

unilateral deflection of the horizontal beam is observed although the onset of the deflection varies in proportion to the thickness of the vertical beams used in the cross-section geometry. Namely, the center vertical beam deflects and bends first, followed by adjacent vertical beams, until a cascading effects occurs to a sufficient extent to induce the horizontal beam unilateral deflection. These deformations are anticipated to correspond to the dynamic energy dissipation mechanisms leveraged by the metamaterial when subjected to impact energy.

Video S6. The R-B metamaterial is subjected to an impact of 150 N on the top surface. The high-speed video capture gives attention to both the middle horizontal beam and the bottommost layer of vertical beams in the metamaterial cross-section to characterize the strain field. The top left quadrant of the video is the unprocessed video images. The top right, bottom left, and bottom right quadrants of the video are the magnitudes of the shear strain $|E_{xy}|$, horizontal normal strain $|E_{xx}|$, and vertical normal strain $|E_{yy}|$, respectively, determined from the DIC post-processing. The video is first played back at 1 s for 10 ms of real-time in two sequences, and then played back at a rate of 1 s for 0.5 ms of real-time. A more mirror symmetric strain profile as well as greater horizontal beam stretching than those similar aspects observed in L-class metamaterials are observed for the R-B metamaterial, exemplifying the primary mechanisms of energy dissipation for the R-class of metamaterial geometry.

Video S7. The L-B metamaterial is subjected to an impact of 151 N on the top surface. The high-speed video capture gives attention to both the middle horizontal beam and the bottommost layer of vertical beams in the metamaterial cross-section to characterize the strain field. The top left quadrant of the video is the unprocessed video images. The top right, bottom left, and bottom right quadrants of the video are the magnitudes of the shear strain $|E_{xy}|$, horizontal normal strain $|E_{xx}|$, and vertical normal strain $|E_{yy}|$, respectively, determined from the DIC post-processing. The video is first played back at 1 s for 10 ms of real-time in two sequences, and then played back at a rate of 1 s for 0.5 ms of real-time. The increased strain localized in the vertical beams and lack of mirror symmetry in the strain profile, as otherwise observed in R-class metamaterials, are seen in the bottom portion of the video, exemplifying the primary mechanisms of energy dissipation for L-class of metamaterial geometry.

Video S8. The R-A metamaterial is compressed in the load frame. The DIC speckle pattern is applied to the metamaterial for sake of the video capture and DIC data post-processing. The top left quadrant of the video is the unprocessed video images. The top right, bottom left, and bottom right quadrants of the video are the magnitudes of the shear strain $|E_{xy}|$, horizontal normal strain $|E_{xx}|$, and vertical normal strain $|E_{yy}|$, respectively, determined from the DIC post-processing. The video is played back at a rate of 1 s for 450 ms of real-time. The bimodal deflection of the horizontal beam and hence greater stretching of the horizontal beam (than the Uniform and L-class metamaterials) are observed in the full field strain data of the DIC output.

Video S9. The L-A metamaterial is compressed in the load frame. The DIC speckle pattern is applied to the metamaterial for sake of the video capture and DIC data post-processing. The top left quadrant of the video is the unprocessed video images. The top right, bottom left, and bottom right quadrants of the video are the magnitudes of the shear strain $|E_{xy}|$, horizontal normal strain $|E_{xx}|$, and vertical normal strain $|E_{yy}|$, respectively, determined from the DIC post-processing. The video is played back at a rate of 1 s for 450 ms of real-time. The

unilateral deflection of the horizontal beam is observed while the onset of the deflection varies in proportion to the thickness of the vertical beams used in the cross-section geometry.

Video S10. The R-A metamaterial is subjected to an impact of 150 N on the top surface. The high-speed video capture gives attention to both the middle horizontal beam and the bottommost layer of vertical beams in the metamaterial cross-section to characterize the strain field. The top left quadrant of the video is the unprocessed video images. The top right, bottom left, and bottom right quadrants of the video are the magnitudes of the shear strain $|E_{xy}|$, horizontal normal strain $|E_{xx}|$, and vertical normal strain $|E_{yy}|$, respectively, determined from the DIC post-processing. The video is first played back at 1 s for 10 ms of real-time in two sequences, and then played back at a rate of 1 s for 0.5 ms of real-time. A less mirror symmetric strain profile than R-B is observed for the R-A metamaterial, although there remains greater horizontal beam stretching than those similar aspects observed in L-class metamaterials.

Video S11. The L-A metamaterial is subjected to an impact of 151 N on the top surface. The high-speed video capture gives attention to both the middle horizontal beam and the bottommost layer of vertical beams in the metamaterial cross-section to characterize the strain field. The top left quadrant of the video is the unprocessed video images. The top right, bottom left, and bottom right quadrants of the video are the magnitudes of the shear strain $|E_{xy}|$, horizontal normal strain $|E_{xx}|$, and vertical normal strain $|E_{yy}|$, respectively, determined from the DIC post-processing. The video is first played back at 1 s for 10 ms of real-time in two sequences, and then played back at a rate of 1 s for 0.5 ms of real-time. The increased strain localized in the vertical beams and lack of mirror symmetry in the strain profile, as otherwise observed in R-class metamaterials, are seen in the bottom portion of the video, exemplifying the primary mechanisms of energy dissipation for L-class of metamaterial geometry.

Video S12. The R-B and L-B metamaterials are subjected to impact forces of applied around 250 N. Three cases of such high-speed video recordings are shown for each metamaterial and played back at a rate of 1 s for 0.5 ms of real-time. The video exemplifies that under high impact loads, the characteristic trend of horizontal deflection symmetry is observed for the R-B metamaterial, while the L-B metamaterial undergoes unilateral buckling and motion of the horizontal beam member. These visual data support the conclusions of this report that impact energy mitigation mechanism are tailored specifically in accordance to the internal geometry of the mechanical metamaterials.